

# Magnetic vortex crystals in frustrated Mott insulator

Y. Kamiya<sup>1</sup> and C. D. Batista<sup>1</sup>

<sup>1</sup>Theoretical Division, T-4 and CNLS, Los Alamos National Laboratory, Los Alamos, New Mexico 87545, USA  
(Dated: March 4, 2013)

The phase diagram near the magnetic field-induced quantum critical point of dimerized spin systems can be extremely rich when the interactions are frustrated. Complex phases that emerge near this critical point are derived under control by mapping the spin system into a dilute gas of bosons. Geometric frustration of the dimer lattice manifests in a rather large degeneracy of wave-vectors  $\mathbf{Q}_n$  that minimize the single-boson dispersion. The bosons can then condense into a single or a multi- $\mathbf{Q}$  state. The magnetic counterparts of these condensates range from a simple spiral (single- $\mathbf{Q}$  condensate) to magnetic vortex crystals (6- $\mathbf{Q}$  condensates). Inspired by the  $S = 1$  dimer antiferromagnet  $\text{Ba}_3\text{Mn}_2\text{O}_8$ , we calculate the effective boson-boson interactions in the dilute limit and demonstrate that a plethora of exotic condensates emerge above the critical field  $H = H_{c1}$  and that a six-fold symmetric exchange anisotropy selects a vortex crystal or a double- $\mathbf{Q}$  fan state.

PACS numbers:

The emergence of topological spin textures in solids triggered an enormous interest because of their relevance for spin-electronic technology. Outstanding examples are the magnetic skyrmion crystals that have been recently observed in specific alloys with B20 structure.<sup>1-3</sup> The helimagnetic ground state of these materials results from competition between ferromagnetic exchange and Dzyaloshinskii-Moriya (DM) interactions. The skyrmion lattice emerges in a narrow temperature and magnetic field window just below the magnetic ordering temperature.<sup>1,2</sup> Last year, Seki *et al.* reported the first discovery of a spontaneous magnetic skyrmion crystal in the insulating chiral magnet  $\text{Cu}_2\text{OSeO}_3$ <sup>4</sup> and opened a new promising route to electric control of magnetism. Helical magnetic orderings, such as skyrmion lattices, induce another texture of electric dipole moments enabling a magneto-electric response that can be exploited to manipulate the magnetic state with electric field gradients.<sup>5</sup> This procedure is energetically more efficient than current-driven approaches required for metals.

After this sequence of discoveries, it is natural to ask if topological spin textures can emerge under more general conditions. In particular, we would like to know if these textures can arise from frustration between exchange interactions instead of competition between the exchange and DM coupling. The advantage of the first mechanism is that the ratio between exchange constants can be changed with pressure, while the ratio between exchange and DM couplings is much less tunable. Thus, the first mechanism enables pressure-induced tuning of the spin texture structural parameters. To explore this exciting possibility, we focus on the field-induced quantum critical point (QCP) of a frustrated spin dimer Mott insulator that is a quantum paramagnet at  $H = 0$ : each dimer is predominantly in its singlet state. The first excitation is a single-dimer triplet state that propagates with well-defined momentum (triplon). The QCP signals the onset of a Bose-Einstein condensate (BEC) of triplons at the field,  $\mathbf{H} = \mathbf{H}_{c1}$ , that closes the single-triplon energy gap.<sup>6</sup> While basic concepts of this transition were established through the study of effectively unfrustrated magnets like  $\text{TiCuCl}_3$ ,<sup>7-9</sup> strongly frustrated materials like  $\text{SrCu}_2(\text{BO}_3)_2$ ,<sup>10-12</sup>  $\text{BaCuSi}_2\text{O}_6$ ,<sup>13-16</sup> and  $\text{Ba}_3\text{Mn}_2\text{O}_8$ <sup>17-22</sup> exhibit more exotic behavior.

$\text{Ba}_3\text{Mn}_2\text{O}_8$  consists of weakly-coupled dimers of  $S = 1$

$\text{Mn}^{5+}$  ( $3d^2$ ) ions that form triangular lattice bilayers stacked along the  $c$  axis in a period-3 structure (Fig. 1). Besides the intra-bilayer exchange, which would alone favor simple three-sublattice commensurate spin orderings,<sup>23</sup> inelastic neutron scattering (INS) measurements<sup>18</sup> revealed several frustrated inter-bilayer exchange constants that shift the single-triplon dispersion minima to six-fold degenerate incommensurate wave-vectors  $\pm\mathbf{Q}_n$  ( $1 \leq n \leq 3$ ) [Fig. 1(d)]. While a simple single- $\mathbf{Q}$  state is stable over a big field interval between  $H_{c1}$  and  $H_{c2}$  ( $H_{c1} \approx 9$  T,  $H_{c2} \approx 26$  T), the observation of a different ordered phase right above  $H_{c1}$ <sup>19</sup> suggests the possibility of an unconventional multi- $\mathbf{Q}$  condensate.

The distribution of the triplon condensate among the six-fold single-triplon dispersion minima is determined by the effective triplon-triplon interaction. Here we consider a hard-core boson model derived from the spin Hamiltonian of  $\text{Ba}_3\text{Mn}_2\text{O}_8$  for  $\mathbf{H} \parallel c$  and  $H \lesssim H_{c1}$ . We use the measured single-triplon dispersion,<sup>18</sup> and vary the triplon-triplon interaction parameters that are more difficult to measure. By expanding in the small lattice gas parameter near the BEC-QCP we predict a rich phase diagram including two different crystals of magnetic vortices among other interesting phases.

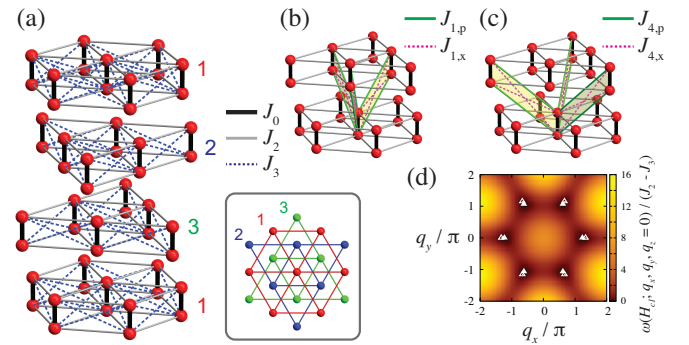


FIG. 1: (a) Magnetic ( $\text{Mn}^{5+}$ ) lattice of  $\text{Ba}_3\text{Mn}_2\text{O}_8$ . (b) Nearest-neighbor (NN) and (c) next-NN inter-bilayer exchange couplings. (d) Single-triplon dispersion. Filled (open) triangles indicate the incommensurate wave-vectors of the lowest-energy modes.

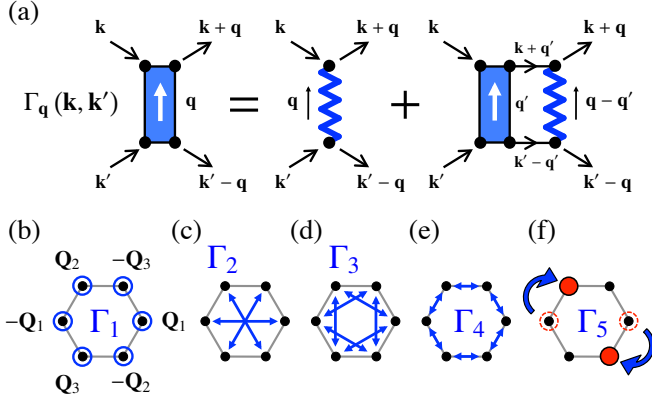


FIG. 2: (a) Effective vertex from ladder diagrams. The wavy line (filled square) represents the bare (effective) potential. (b)–(f) Effective interactions in the Ginzburg-Landau theory.

### FRUSTRATED HARD-CORE BOSON MODEL

The  $S = 1$  spin Hamiltonian of  $\text{Ba}_3\text{Mn}_2\text{O}_8$  is defined on the lattice depicted in Fig. 1.<sup>21</sup> The intra-dimer antiferromagnetic exchange,  $J_0 \approx 19.05(4)$  K,<sup>18</sup> is much bigger than any inter-dimer exchange. The single-dimer low-energy sector is conveniently described with bosonic bond operators,<sup>24,25</sup> that create singlet,  $s_i^\dagger|\emptyset\rangle_i$ , and triplet states,  $t_{i,\sigma}^\dagger|\emptyset\rangle_i$  ( $\sigma = 1, 0, \bar{1}$ ), in each dimer  $i$  and satisfy the constraint  $s_i^\dagger s_i + \sum_\sigma t_{i,\sigma}^\dagger t_{i,\sigma} = 1$ . Spin-2 states can be ignored near  $H = H_{c1}$  because they do not modify the triplon dispersion to lowest order in the inter-dimer exchange. At the mean field level, the paramagnetic state for  $H \leq H_{c1}$  is described as a singlet condensate:  $s_i^\dagger = s_i = 1$ .<sup>25,26</sup> The resulting Hamiltonian has a quadratic contribution in the triplet operators that is diagonalized in momentum space,  $t_{\mathbf{k},\sigma}^\dagger = N^{-1/2} \sum_i \exp(i\mathbf{k} \cdot \mathbf{r}_i) t_{i,\sigma}^\dagger$  ( $N$  is the number of dimers), by a standard Bogoliubov transformation:<sup>22</sup>

$$\mathcal{H}_2 = \sum_{\mathbf{k}} \omega_{\mathbf{k}} \left( \tau_{\mathbf{k}}^\dagger \tau_{\mathbf{k}} + \frac{1}{2} \right) - \frac{1}{2} \sum_{\mathbf{k}} \epsilon_{\mathbf{k}}, \quad \omega_{\mathbf{k}} = \sqrt{\epsilon_{\mathbf{k}}^2 - \gamma_{\mathbf{k}}^2} - g\mu_B H, \quad \epsilon_{\mathbf{k}} = J_0 - \frac{D}{3} + \gamma_{\mathbf{k}}. \quad (1)$$

$\mathcal{H}_2$  includes only the lowest energy  $S^z = 1$  single-triplon branch:  $\tau_{\mathbf{k}}$  is the  $S^z = 1$  Bogoliubov quasi-particle (dressed triplon) that becomes soft at  $H = H_{c1}$  and  $\omega_{\mathbf{k}}$  is the single-triplon dispersion.  $\gamma_{\mathbf{k}} = (8/3)[(J_2 - J_3)\tilde{\gamma}_{\mathbf{k}}^{(2)} + (J_{1,p} - J_{1,x})\tilde{\gamma}_{\mathbf{k}}^{(1)} + (J_{4,p} - J_{4,x})\tilde{\gamma}_{\mathbf{k}}^{(4)}]$  is the bare triplon dispersion where  $\tilde{\gamma}_{\mathbf{k}}^{(2)} = \cos k_1 + \cos k_2 + \cos(k_1 - k_2)$ ,  $\tilde{\gamma}_{\mathbf{k}}^{(1)} = \cos k_3 + \cos(k_3 - k_1) + \cos(k_3 - k_2)$ , and  $\tilde{\gamma}_{\mathbf{k}}^{(4)} = \cos(-k_1 + k_2 + k_3) + \cos(k_1 - k_2 + k_3) + \cos(k_1 + k_2 - k_3)$ . The intra-layer triplon hopping amplitude is proportional to  $J_2 - J_3 \approx 1.318(8)$  K, where  $J_2$  and  $J_3$  are the nearest-neighbor (NN) intra-bilayer exchange couplings along parallel and cross paths, respectively. We include both parallel- and cross-path couplings in the NN ( $J_{1,p}$  and  $J_{1,x}$ ) and next-NN inter-bilayer exchanges ( $J_{4,p}$  and  $J_{4,x}$ ) [Figs. 1(b) and 1(c)]. INS results indicate

$J_{1,p} - J_{1,x} \approx -0.685(10)$  K and  $J_{4,p} - J_{4,x} \approx -0.215(10)$  K.<sup>18</sup> The inter-layer triplon hopping amplitudes are proportional to these differences and they are responsible for the in-plane shifts of the  $\omega_{\mathbf{k}}$  minima from the two commensurate three-sublattice ordering wave-vectors (2D limit) to the six wave-vectors shown in Fig. 1(d):  $\mathbf{Q}_1 = (2\alpha, \alpha, \alpha)$ ,  $\mathbf{Q}_2 = (-\alpha, \alpha, 0)$ ,  $\mathbf{Q}_3 = (-\alpha, -2\alpha, -\alpha)$ ,  $-\mathbf{Q}_1$ ,  $-\mathbf{Q}_2$ , and  $-\mathbf{Q}_3$  with

$$\alpha = \arccos \left[ -\frac{1}{2} \frac{J_2 - J_3 + J_{1,p} - J_{1,x}}{J_2 - J_3 + 2(J_{4,p} - J_{4,x})} \right] \approx \frac{2\pi}{3} \times 0.924(5). \quad (2)$$

The boson-boson interaction terms are

$$\begin{aligned} \mathcal{H}_4 &= \frac{1}{2N} \sum_{\mathbf{k}, \mathbf{k}', \mathbf{q}} (U + V_{\mathbf{q}}) \tau_{\mathbf{k}+\mathbf{q}}^\dagger \tau_{\mathbf{k}'-\mathbf{q}}^\dagger \tau_{\mathbf{k}'} \tau_{\mathbf{k}}, \\ V_{\mathbf{q}} &= 2 \left( V_2 \tilde{\gamma}_{\mathbf{k}}^{(2)} + V_1 \tilde{\gamma}_{\mathbf{k}}^{(1)} + V_4 \tilde{\gamma}_{\mathbf{k}}^{(4)} \right), \quad V_2 = (J_2 + J_3)/2, \\ V_1 &= (J_{1,p} + J_{1,x})/2, \quad V_4 = (J_{4,p} + J_{4,x})/2. \end{aligned} \quad (3)$$

Here we used that  $\tau_{\mathbf{k}} \approx t_{\mathbf{k},1}$  in the low-density limit. The local constraint  $s_i^\dagger s_i + \sum_\sigma t_{i,\sigma}^\dagger t_{i,\sigma} = 1$  is imposed by including an on-site hard-core potential  $U \rightarrow \infty$ .<sup>25</sup>  $V_1$ ,  $V_2$ , and  $V_4$  are the off-site interactions determined by the exchange constants. In the long wave-length limit,  $\mathbf{k} \approx \pm \mathbf{Q}_n$ , the effective triplon-triplon interaction is obtained by adding the ladder diagrams shown in Fig. 2(a).<sup>27–30</sup> The resulting interaction vertex  $\Gamma_{\mathbf{q}}(\mathbf{k}, \mathbf{k}')$  for incoming particles with momenta  $\mathbf{k}$  and  $\mathbf{k}'$  and the momentum transfer  $\mathbf{q}$  is asymptotically exact in the dilute limit  $H \approx H_{c1}$ . (The computation of  $\Gamma_{\mathbf{q}}(\mathbf{k}, \mathbf{k}')$  is described in Methods A.)

### GINZBURG-LANDAU THEORY

If  $N^{-1/2} \langle \tau_{\pm \mathbf{Q}_n} \rangle \equiv \sqrt{\rho_{\pm \mathbf{Q}_n}} \exp(i\phi_{\pm \mathbf{Q}_n})$  is the condensate wave function of the lowest-energy mode  $\pm \mathbf{Q}_n$  ( $1 \leq n \leq 3$ ), the triplon density is  $\rho \equiv \sum_n (\rho_{\mathbf{Q}_n} + \rho_{-\mathbf{Q}_n})$  ( $\ll 1$ ) and the Ginzburg-Landau (GL) expansion of the ground state energy density is

$$\begin{aligned} E_{\text{eff}} &= -\mu \sum_n (\rho_{\mathbf{Q}_n} + \rho_{-\mathbf{Q}_n}) + \frac{\Gamma_1}{2} \sum_n (\rho_{\mathbf{Q}_n}^2 + \rho_{-\mathbf{Q}_n}^2) \\ &+ \Gamma_2 \sum_n \rho_{\mathbf{Q}_n} \rho_{-\mathbf{Q}_n} + \Gamma_3 \sum_{n < m} (\rho_{\mathbf{Q}_n} \rho_{\mathbf{Q}_m} + \rho_{-\mathbf{Q}_n} \rho_{-\mathbf{Q}_m}) \\ &+ \Gamma_4 \sum_{n < m} (\rho_{\mathbf{Q}_n} \rho_{-\mathbf{Q}_m} + \rho_{-\mathbf{Q}_n} \rho_{\mathbf{Q}_m}) \\ &+ 2\Gamma_5 \sum_{n < m} \sqrt{\rho_{\mathbf{Q}_n} \rho_{-\mathbf{Q}_n} \rho_{\mathbf{Q}_m} \rho_{-\mathbf{Q}_m}} \cos(\Phi_n - \Phi_m), \end{aligned} \quad (4)$$

where  $\mu = g\mu_B(H - H_{c1})$  and  $\Phi_n \equiv \phi_{\mathbf{Q}_n} + \phi_{-\mathbf{Q}_n}$ . The coefficients are obtained by replacing the bare interactions in  $\mathcal{H}_4$  by the effective interaction vertices:

$$\begin{aligned} \Gamma_1 &= \Gamma_0(\mathbf{Q}_n, \mathbf{Q}_n), \quad \Gamma_2 = \Gamma_0(\mathbf{Q}_n, -\mathbf{Q}_n) + \Gamma_{-2\mathbf{Q}_n}(\mathbf{Q}_n, -\mathbf{Q}_n), \\ \Gamma_3 &= \Gamma_0(\mathbf{Q}_n, \mathbf{Q}_m) + \Gamma_{\mathbf{Q}_m - \mathbf{Q}_n}(\mathbf{Q}_n, \mathbf{Q}_m) \quad (n \neq m), \\ \Gamma_4 &= \Gamma_0(\mathbf{Q}_n, -\mathbf{Q}_m) + \Gamma_{-\mathbf{Q}_m - \mathbf{Q}_n}(\mathbf{Q}_n, -\mathbf{Q}_m) \quad (n \neq m), \\ \Gamma_5 &= \Gamma_{\mathbf{Q}_m - \mathbf{Q}_n}(\mathbf{Q}_n, -\mathbf{Q}_n) + \Gamma_{-\mathbf{Q}_m - \mathbf{Q}_n}(\mathbf{Q}_n, -\mathbf{Q}_n) \quad (n \neq m). \end{aligned} \quad (5)$$

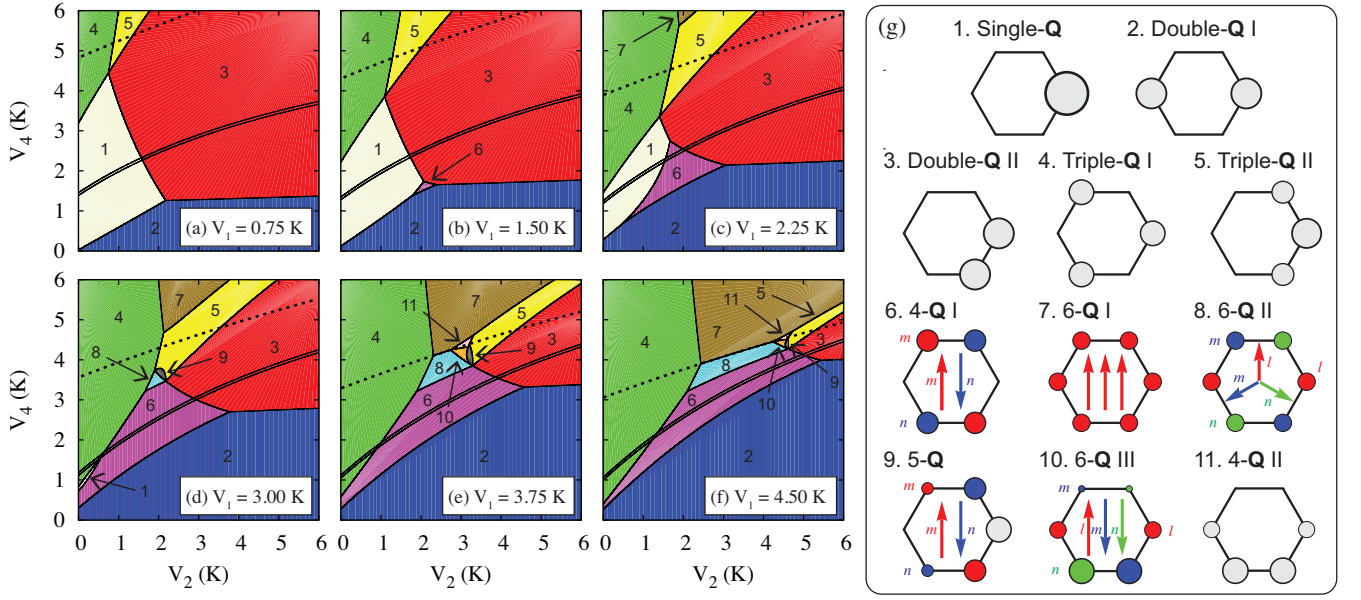


FIG. 3: (a)–(f) The ground state phase diagram at the BEC-QCP as a function of the bare interaction potentials  $V_1$ ,  $V_2$ , and  $V_4$ . The dashed line indicates a boundary above (below) which  $\Gamma_5 < 0$  ( $> 0$ ), while the double line shows a phase boundary between the state No. 2 (below) and No. 8 (above) when weak anisotropic perturbations are taken into account (see text). (g) Schematic pictures of the condensate distributions among  $\pm \mathbf{Q}_n$  ( $1 \leq n \leq 3$ ). The arrows representing  $\Phi_n \equiv \phi_{\mathbf{Q}_n} + \phi_{-\mathbf{Q}_n}$  are shown only for those states with particular conditions for  $\Phi_n$ .

Most terms in (4) are density-density interactions [Figs. 2(b)–2(e)]. Only the  $\Gamma_5$  term of the off-diagonal form  $\tau_{\mathbf{Q}_m}^\dagger \tau_{-\mathbf{Q}_m} \tau_{\mathbf{Q}_n} \tau_{-\mathbf{Q}_n}$  ( $n \neq m$ ) is sensitive to the relative phases  $\Phi_n - \Phi_m$  [Fig. 2(f)].

The phase diagram near the BEC-QCP is obtained by minimization of  $E_{\text{eff}}$  (4) at constant- $\rho$  as a function of  $V_1$ ,  $V_2$ , and  $V_4$  (Fig. 3). We restrict our attention to the region  $0 \leq V_1, V_2, V_4 \ll J_0$ , which is appropriate for weakly-coupled dimer systems with repulsive triplon-triplon interactions.  $\Gamma_1$ ,  $\Gamma_2$ ,  $\Gamma_3$ , and  $\Gamma_4$  are positive in this regime. Only  $\Gamma_5$  changes its sign on the dashed  $\Gamma_5 = 0$  line shown in Fig. 3. The GL expansion (4) is justified because the transition is always continuous for the region of interest ( $|\Gamma_5| \ll \Gamma_\nu$ ,  $1 \leq \nu \leq 4$ ).

The phase diagram of Fig. 3 includes eleven phases that are schematically represented in Fig. 3(g). (The precise wave functions are summarized in Table I in Methods.) The magnetic orderings are better described in terms of  $S = 1/2$  pseudospin variables  $\mathbf{s}_i$  obtained from a Matsubara-Matsuda transformation:<sup>31</sup>  $s_i^z \leftrightarrow 1/2 - t_{i,1}^\dagger t_{i,1}$  and  $s_i^\pm (s_i^\mp) \leftrightarrow t_{i,1} (t_{i,1}^\dagger)$ . The BEC state for  $H > H_{c1}$  is well approximated by the mean field state  $|\Psi\rangle \approx \prod_i [\cos(\theta_i/2) s_i^\dagger |\emptyset\rangle_i + \sin(\theta_i/2) e^{i\varphi_i} t_{i,1}^\dagger |\emptyset\rangle_i]$ , which is a direct product of spin coherent states in terms of the  $s$  variables. The relations between spin and pseudospin expectation values are

$$\langle S_{i,\mu}^\pm \rangle = (-1)^\mu \frac{2}{\sqrt{3}} \langle s_i^\mp \rangle, \quad \langle S_{i,\mu}^z \rangle = \frac{1}{4} (1 - 2\langle s_i^\mp \rangle), \quad (6)$$

where  $\mu = 1, 2$  labels each spin of the dimer  $i$ .

## SINGLE-Q STATE AND ITS INSTABILITIES

The simplest ordered phase is the single-Q state (No. 1). The  $xy$  pseudospin components spiral around a uniform  $z$ -component (cone structure). Our analysis of (4) shows that this phase is stable in a region where  $V_1$ ,  $V_2$ , and  $V_4$  are smaller or comparable to a characteristic energy scale  $2t_\perp = (8/3)(J_2 - J_3) \approx 3.52(2)$  K, where  $t_\perp$  is the intra-layer triplon hopping amplitude. The occupation of a single mode requires  $\Gamma_1 < \min(\Gamma_2, \Gamma_3, \Gamma_4)$ . For instance, the state No. 2, in which two modes  $\pm \mathbf{Q}_n$  are evenly occupied, has lower energy for  $\Gamma_1 > \Gamma_2$ . The corresponding spin configuration has a fan-like coplanar spatial modulation. Likewise, the condition  $\Gamma_1 = \Gamma_4$  induces an instability to the state No. 3, in which  $\mathbf{Q}_n$  and  $-\mathbf{Q}_m$  ( $n \neq m$ ) are evenly occupied. This state also exhibits the fan-type spatial modulation with wave-vector  $(\mathbf{Q}_n + \mathbf{Q}_m)/2$ , but the fan-plane rotates with a different wave-vector  $(\mathbf{Q}_n - \mathbf{Q}_m)/2$ .

The single-Q state also becomes unstable for  $\Gamma_1 \geq \Gamma_3$ . In this case, the energy is minimized by distributing the condensate over  $\{\mathbf{Q}_1, \mathbf{Q}_2, \mathbf{Q}_3\}$  or  $\{-\mathbf{Q}_1, -\mathbf{Q}_2, -\mathbf{Q}_3\}$ . Figure 4(c) shows the resulting triple-Q state (No. 4) that is a triangular superstructure of magnetic domains with a local approximate  $120^\circ$   $xy$ -order. The phase difference between different domains is  $\pm 2\pi/3$ , where the  $\pm$  sign distinguishes the two possible staggered chiralities of the spin superstructure. The local  $120^\circ$  order results from proximity of  $\pm \mathbf{Q}_n$  to the commensurate three-sublattice wave-vectors (weak inter-bilayer exchange) [Eq. (2) or Fig. 1(d)]. The lattice spacing  $a^*$  of the spin superstructure is controlled by the small shift from the commensurate wave-vectors:  $a^* = \sqrt{3}|1 - 3\alpha/(2\pi)|^{-1} \approx 23(2)$ . Around each



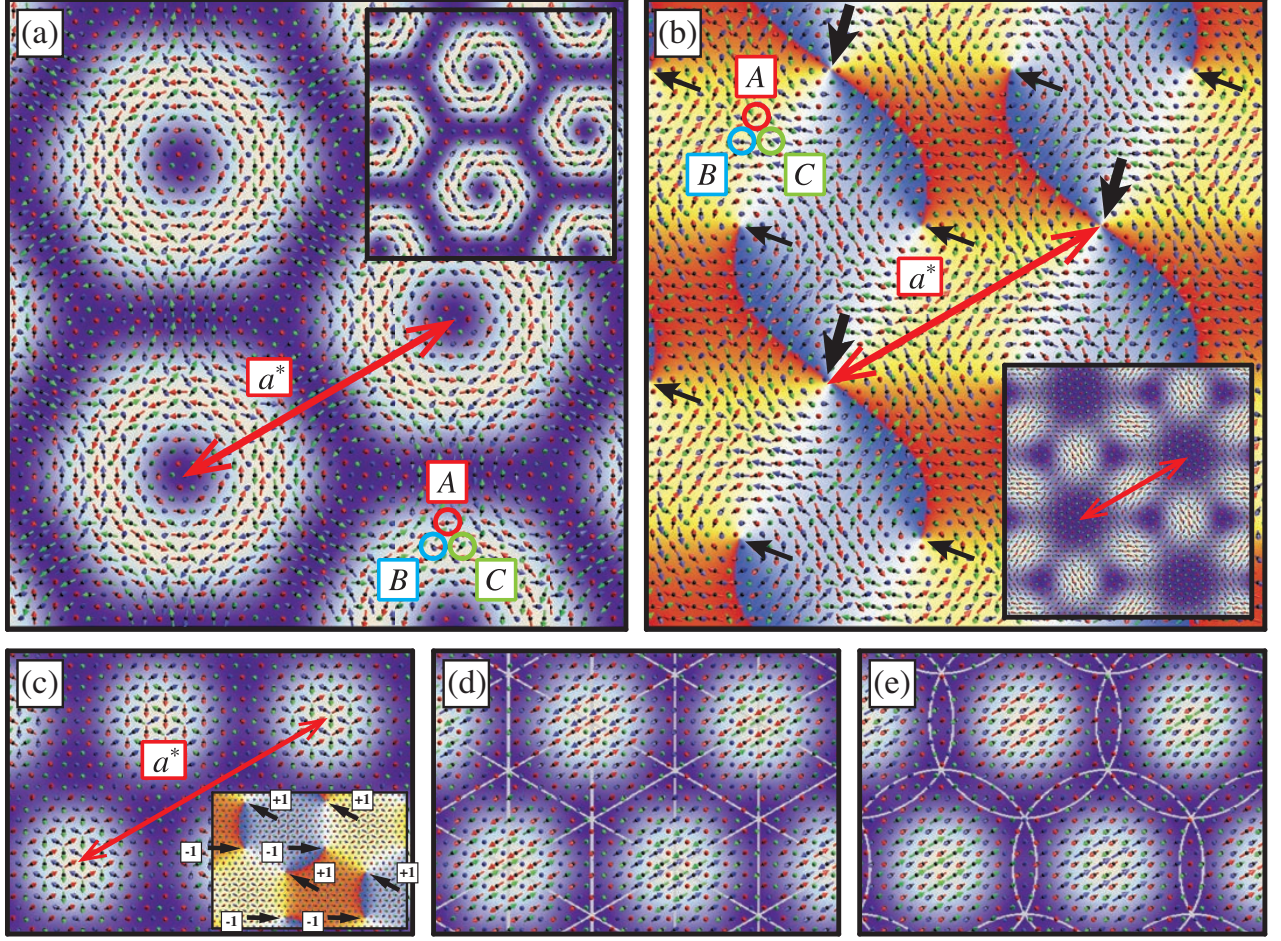


FIG. 4: Spin configurations of some ordered states: (a) No. 8 ( $\Theta = \pi$ ,  $\kappa = +1$ ), (b) No. 8 ( $\Theta = 0$ ,  $\kappa = +1$ ), (c) No. 4, (d) No. 7 ( $\Theta = \pi$ ), and (e) No. 7 ( $\Theta = 0$ ). To emphasize the long wave-length modulation we define the sublattice wave function  $\psi_X(\mathbf{r}) = \sum_n [c_n \exp[i(\Delta\mathbf{Q}_n \cdot \mathbf{r}_i + \chi_{X,n})] + \bar{c}_n \exp[-i(\Delta\mathbf{Q}_n \cdot \mathbf{r}_i + \chi_{X,n})]]$  and  $\rho_X(\mathbf{r}) \equiv |\psi_X(\mathbf{r})|^2$  for  $X = A, B$ , and  $C$ , where  $\Delta\mathbf{Q}_n \equiv [1 - 2\pi/(3\alpha)]\mathbf{Q}_n$  is a shift of  $\mathbf{Q}_n$  from the closest wave-vector of the three-sublattice commensurate order and  $\chi_{X,n}$  are phase factors ensuring  $\psi_X(\mathbf{r}_i) = \langle \tau_i \rangle$  for every site  $i$  on each sublattice  $X$ .  $c_n$  and  $\bar{c}_n$  are given in Table I in Methods. We show  $\rho_A(\mathbf{r})$  in (a) and (c) [ $\rho_A \approx \rho_B \approx \rho_C$  in (c); the inset of (c) shows  $\text{Arg} \psi_A(\mathbf{r})$ ,  $\text{Arg} \psi_B(\mathbf{r})$  in (b) ( $\rho_A(\mathbf{r})$  in the inset), and  $\rho_{\max}(\mathbf{r}) \equiv \max[\rho_A(\mathbf{r}), \rho_B(\mathbf{r}), \rho_C(\mathbf{r})]$  in (d) and (e). The large and small thick arrows in (b) indicate vortices on the  $A$  sublattice with vorticity -2 and +1 respectively. The double anti-vortices are located at the centers of the large dark spots in the inset, while the single vortices are at the center of the small dark spots. The inset of (a) illustrates the same ordered state for a small value of  $|\mathbf{Q}_n|$ .

domain there are vortices and antivortices that form a honeycomb lattice [inset of Fig. 4(c)]. We will discuss more examples of vortex crystals in the next section.

### QUANTUM VORTEX CRYSTALS

The states so far discussed occupy less than four modes, meaning that the  $\Gamma_5$  term has no contribution to the energy density. Our phase diagram suggests that states involving  $\Gamma_5$  require amplitudes  $V_1, V_2, V_4$  that are comparable to the kinetic energy. Among such states, we next discuss the state (No. 8) in which the six modes are equally occupied and the phase parameters satisfy  $\Phi_n^\kappa = -2\kappa n\pi/3 + \text{const.}$  to minimize the energy for  $\Gamma_5 > 0$  (see Methods B). Here  $\kappa = \pm 1$  is a chiral order parameter. This phase becomes unstable towards state

No. 7 at the  $\Gamma_5 = 0$  line [Figs. 3(e) and 3(f)]. The new state is also characterized by equally occupied six modes but the phase variables are the same because  $\Gamma_5 < 0$ :  $\Phi_1 = \Phi_2 = \Phi_3$ . A close examination of the wave functions of states 7, 8, and 10 reveals an additional U(1)-invariant parameter,

$$\Theta \equiv \sum_n (\phi_{\mathbf{Q}_n} - \phi_{-\mathbf{Q}_n}) = 0, \pi, \quad (7)$$

that distinguishes between the spin structures shown in Figs. 4(a) and 4(b). The energy dependence on  $\Theta$  is a consequence of a three-body process of the form

$$\begin{aligned} \mathcal{H}_6 &\propto \tau_{\mathbf{Q}_1}^\dagger \tau_{\mathbf{Q}_2}^\dagger \tau_{\mathbf{Q}_3}^\dagger \tau_{-\mathbf{Q}_1} \tau_{-\mathbf{Q}_2} \tau_{-\mathbf{Q}_3} + \text{H.c.} \\ &\sim 2 \sqrt{\prod_n \rho_{\mathbf{Q}_n} \rho_{-\mathbf{Q}_n}} \cos \Theta. \end{aligned} \quad (8)$$

The sign of the prefactor determines the value of  $\Theta$ . We will then discuss the two cases  $\Theta = 0, \pi$ . By properly choosing  $\mathbf{r}^*$  (not restricted to lattice sites), the spin configuration can be rewritten as

$$\langle s_i^+ \rangle_{\kappa, \Theta} = \sqrt{\frac{2\rho}{3}} \sum_n \cos \left[ \mathbf{Q}_n \cdot (\mathbf{r}_i - \mathbf{r}^*) + \delta_{n,3} \frac{\Theta}{2} \right] e^{i\Phi_n^\kappa/2}. \quad (9)$$

Figure 4(a) shows that this 6- $\mathbf{Q}$  state for  $\Theta = \pi$  is a crystallization of a magnetic vortices in a triangular superlattice. The crystallized vortices are not topological defects but thermodynamic stable states similar to the crystallizations of skyrmions,<sup>1,3,4,32</sup>  $Z_2$  vortices,<sup>33</sup> and solitons,<sup>34–36</sup> or the Abrikosov lattices in the type-II superconductors.<sup>37</sup> In the present case, the vortex texture appears in each of the three underlying sublattices ( $A$ ,  $B$ , and  $C$ ) because of proximity of  $\pm \mathbf{Q}_n$  to the commensurate three-sublattice order wave-vectors. The triplon density is 0 or nearly 0 at the vortex cores and on the boundaries between adjacent vortices. The vortex crystal is chiral because all the vortices have the same value of  $\kappa$ . The lattice spacing of each vortex sublattice is  $a^* = \sqrt{3}|1 - 3\alpha/(2\pi)|^{-1}$ . The three sublattice structure disappears for  $|\mathbf{Q}_n| \approx 0$  leading to a simple triangular vortex crystal [see inset of Fig. 4(a)].

Figure 4(b) illustrates the other vortex crystal obtained for  $\Theta = 0$ . The triangular vortex lattice has three sublattices. Two sublattices are occupied by single vortices ( $\kappa = \pm 1$ ), while the third sublattice is occupied by double-antivortices ( $\kappa = \mp 2$ ). States 5, 6, 9, 10, and 11 correspond to other vortex crystal structures.

The above mentioned phase No. 7 is a 6- $\mathbf{Q}$  state with a coplanar fan-like modulation [Figs. 4(d) and 4(e)]. The fan-plane is determined by the angle  $\Phi/2$ , where  $\Phi = \Phi_1 = \Phi_2 = \Phi_3$ . The spin configuration is obtained by replacing  $\Phi_n^\kappa$  with  $\Phi$  in Eq. (9) and it is slightly different for  $\Theta = 0, \pi$ . Both cases correspond to a triangular superlattice of magnetic domains similar to state No. 4, but the present states exhibit local coplanar order in each domain. The local order for  $\Theta = \pi$  comprises three pseudospins, one of which is almost polarized and the other two are canted in opposite directions [Fig. 4(d)]. In contrast, the local order for  $\Theta = 0$  comprises two pseudospins canted in the same direction while the third one is canted in the opposite direction [Fig. 4(e)].

## EFFECTS OF ANISOTROPY

The  $U(1)$  symmetry of our Hamiltonian for  $\mathbf{H} \parallel c$  is always broken down to the six-fold symmetry of the triangular lattice when exchange anisotropy induced by spin-orbit or dipole-dipole interactions is included. In the long wave-length limit, the contribution of this exchange anisotropy is

$$\begin{aligned} \mathcal{H}_{\text{anis}} &\propto \sum_n (\tau_{\mathbf{Q}_n}^\dagger \tau_{-\mathbf{Q}_n}^\dagger e^{2(n-1)\pi i/3} + \text{H.c.}) \\ &\sim \sum_n 2\sqrt{\rho_{\mathbf{Q}_n}\rho_{-\mathbf{Q}_n}} \cos\left(\Phi_n - \frac{2(n-1)\pi}{3}\right). \end{aligned} \quad (10)$$

While the exchange anisotropy is small compared to the exchange interactions in  $\text{Ba}_3\text{Mn}_2\text{O}_8$ , this term becomes the dominant contribution very close to the QCP because *it is linear in  $\rho$* , while the interaction terms included in Eq. (4) are quadratic. Interestingly enough, among the competing phases that appear in the phase diagram of Fig. 3 this term stabilizes the double- $\mathbf{Q}$  fan state (No. 2) and the vortex crystals (6- $\mathbf{Q}$  condensate No. 8 with  $\Theta = 0$  or  $\Theta = \pi$ ).  $\mathcal{H}_{\text{anis}}$  favors one of the two chiralities ( $\kappa = -1$ ) of the the vortex crystal with net chirality. Then, the main role of the interaction terms (4) right above  $H_{c1}$  is to split the degeneracy between these two different spin orderings. The resulting phase boundary (double line in Fig. 3) is obtained from the condition  $2(\Gamma_1 + \Gamma_2 - \Gamma_3 - \Gamma_4) + \Gamma_5 = 0$ .

A different source of anisotropy appears when  $\mathbf{H}$  is tilted away from the six-fold symmetry  $c$  axis because of a small single-ion anisotropy  $D \approx -0.28$  K along the  $c$ -axis that breaks the six-fold symmetry into  $Z_2$ <sup>19,38</sup> and leads to the following long wave-length contribution:

$$\mathcal{H}_{Z_2} \propto \sum_n (\tau_{\mathbf{Q}_n}^\dagger \tau_{-\mathbf{Q}_n}^\dagger + \text{H.c.}) \sim \sum_n 2\sqrt{\rho_{\mathbf{Q}_n}\rho_{-\mathbf{Q}_n}} \cos \Phi_n. \quad (11)$$

This term alone favors the coplanar states No. 2 or No. 7. The boundary between these phases,  $\Gamma_1 + \Gamma_2 - \Gamma_3 - \Gamma_4 - \Gamma_5 = 0$ , is again determined by the triplon-triplon interaction (4). The maximum amplitude of  $\mathcal{H}_{Z_2}$  ( $\mathbf{H} \perp c$ ) is comparable to the amplitude of  $\mathcal{H}_{\text{anis}}$  and the competition between these terms is controlled by the angle between  $\mathbf{H}$  and the  $c$  axis.

Thermodynamic measurements on  $\text{Ba}_3\text{Mn}_2\text{O}_8$  show two different phases in the vicinity of  $H = H_{c1}$  even for  $\mathbf{H} \parallel c$ .<sup>21</sup> A narrow Phase II that appears right above  $H_{c1}$  and a broad Phase I, which is a single- $\mathbf{Q}$  spiral, extends over a much bigger window of magnetic fields. The fact that the double line shown in Fig. 3 crosses the single- $\mathbf{Q}$  phase indicates that both possible scenarios could explain Phase II when the angle between  $\mathbf{H}$  and the  $c$  axis is small: it is either the double- $\mathbf{Q}$  fan state or a vortex crystal. This prediction can be verified by performing nuclear magnetic resonance (NMR) or neutron scattering experiments right above  $H = H_{c1}$ .

It is important to emphasize that our conclusions extend beyond the particular case of  $\text{Ba}_3\text{Mn}_2\text{O}_8$ . In general, six-fold symmetric frustrated magnets that exhibit six degenerate minima in the single-triplon dispersion (for quantum dimer systems) or in the single-magnon dispersion above the saturation field (for usual magnets) should either exhibit a double- $\mathbf{Q}$  fan state or a vortex crystal close enough to the critical field. Therefore, the field induced magnetic vortex crystals should be rather ubiquitous in these materials.

## METHODS A: Computation of $\Gamma_{\mathbf{q}}(\mathbf{k}, \mathbf{k}')$

The Bethe-Salpeter equation for  $\Gamma_{\mathbf{q}}(\mathbf{k}, \mathbf{k}')$  corresponding to a zero total frequency ladder diagram is

$$\Gamma_{\mathbf{q}}(\mathbf{k}, \mathbf{k}') = U + V_{\mathbf{q}} - \int \frac{d^3 q'}{8\pi^3} \frac{\Gamma_{\mathbf{q}'}(\mathbf{k}, \mathbf{k}') (U + V_{\mathbf{q}-\mathbf{q}'})}{\omega_{\mathbf{k}+\mathbf{q}'} + \omega_{\mathbf{k}'-\mathbf{q}'}}. \quad (\text{A1})$$

Below we simplify our notation as  $\Gamma_{\mathbf{q}} \equiv \Gamma_{\mathbf{q}}(\mathbf{k}, \mathbf{k}')$ . We will show that in lattice models (A1) can be reduced to coupled linear equations by using the following ansatz:

$$\Gamma_{\mathbf{q}} = \int \frac{d^3 q'}{8\pi^3} \Gamma_{\mathbf{q}'} + \sum_{\eta=1}^z A_{\eta} V(\mathbf{r}_{\eta}) e^{i\mathbf{q} \cdot \mathbf{r}_{\eta}}. \quad (\text{A2})$$

Here  $\mathbf{r}_{\eta}$  denotes a displacement vector to a site within a range of the interaction potential,  $z$  is the total number of such vectors, and  $A_{\eta} \equiv A_{\eta}(\mathbf{k}, \mathbf{k}')$  are the coefficients to be determined.

Since  $\int d^3 q' V_{\mathbf{q}'} = 0$ , we find

$$\langle \Gamma \rangle \equiv \int \frac{d^3 q'}{8\pi^3} \Gamma_{\mathbf{q}'} = U \left( 1 - \int \frac{d^3 q'}{8\pi^3} \frac{\Gamma_{\mathbf{q}'}}{\omega_{\mathbf{k}+\mathbf{q}'} + \omega_{\mathbf{k}'-\mathbf{q}'}} \right). \quad (\text{A3})$$

Then, we rewrite (A1) as

$$\Gamma_{\mathbf{q}} = \langle \Gamma \rangle + V_{\mathbf{q}} - \int \frac{d^3 q'}{8\pi^3} \frac{\Gamma_{\mathbf{q}'} V_{\mathbf{q}-\mathbf{q}'}}{\omega_{\mathbf{k}+\mathbf{q}'} + \omega_{\mathbf{k}'-\mathbf{q}'}}}, \quad (\text{A4})$$

and introduce the following notation:

$$\begin{aligned} \tau_0 &\equiv \int \frac{d^3 q'}{8\pi^3} \frac{1}{\omega_{\mathbf{k}+\mathbf{q}'} + \omega_{\mathbf{k}'-\mathbf{q}'}}}, \quad \tau_1^{\eta} \equiv \int \frac{d^3 q'}{8\pi^3} \frac{e^{-i\mathbf{q}' \cdot \mathbf{r}_{\eta}}}{\omega_{\mathbf{k}+\mathbf{q}'} + \omega_{\mathbf{k}'-\mathbf{q}'}}}, \\ \tau_2^{\eta, \nu} &\equiv \int \frac{d^3 q'}{8\pi^3} \frac{e^{-i\mathbf{q}' \cdot (\mathbf{r}_{\eta} - \mathbf{r}_{\nu})}}{\omega_{\mathbf{k}+\mathbf{q}'} + \omega_{\mathbf{k}'-\mathbf{q}'}}}. \end{aligned} \quad (\text{A5})$$

By substituting (A2) into (A3), we obtain

$$\sum_{\eta=1}^z V(\mathbf{r}_{\eta}) (\tau_1^{\eta})^* A_{\eta} + (\tau_0 + U^{-1}) \langle \Gamma \rangle = 1, \quad (\text{A6})$$

We can now safely take the  $U \rightarrow \infty$  limit. The substitution of (A2) into (A4) leads to

$$\sum_{\nu=1}^z (\tau_2^{\eta, \nu} V(\mathbf{r}_{\nu}) + \delta_{\eta, \nu}) A_{\nu} + \tau_1^{\eta} \langle \Gamma \rangle = 1, \quad 1 \leq \eta \leq z. \quad (\text{A7})$$

These equations can be made compact in a matrix form:

$$\begin{pmatrix} B_{11} & \dots & B_{1z} & \tau_1^1 \\ \vdots & \ddots & \vdots & \vdots \\ B_{z1} & \dots & B_{zz} & \tau_1^z \\ c_1 & \dots & c_z & \tau_0 \end{pmatrix} \begin{pmatrix} A_1 \\ \vdots \\ A_z \\ \langle \Gamma \rangle \end{pmatrix} = \begin{pmatrix} 1 \\ \vdots \\ 1 \\ 1 \end{pmatrix}, \quad (\text{A8})$$

where  $B_{\eta\nu} \equiv \tau_2^{\eta\nu} V(\mathbf{r}_{\nu}) + \delta_{\eta, \nu}$  and  $c_{\eta} \equiv V(\mathbf{r}_{\eta}) (\tau_1^{\eta})^*$ . Since the matrix elements in the left hand side are  $\mathbf{q}$ -independent,  $A_{\eta}$  ( $1 \leq \eta \leq z$ ) and  $\langle \Gamma \rangle$  are also  $\mathbf{q}$ -independent as is assumed in the ansatz (A2). While the lattice symmetry may be used to simplify Eq. (A8), this is a generic prescription for solving the integral equation (A1) for lattice models.

## METHODS B: Determination of $\Phi_n$

The vortex lattice (No. 8) and the state No. 10 require special relations for  $\Phi_n$  ( $1 \leq n \leq 3$ ). The relative relative phases

are determined by the condensate densities  $\rho_{\pm \mathbf{Q}_n}$  ( $1 \leq n \leq 3$ ) through the term  $\Gamma_5$  in Eq. (4) as is outlined below. We assume  $\rho_{\pm \mathbf{Q}_n} \neq 0, \forall n$ , because otherwise a condition for  $\Phi_n$  follows in a trivial way. It is also easy to verify that the case with  $\Gamma_5 < 0$  leads to  $\Phi_1 = \Phi_2 = \Phi_3$ . Thus we consider  $\Gamma_5 > 0$  below.

We can rewrite the term  $\Gamma_5$  by fixing the global U(1) phase at  $\Phi_3 = 0$ :

$$E_{\text{eff},5} = 2\Gamma_5 \sqrt{\rho_{\mathbf{Q}_1} \rho_{-\mathbf{Q}_1} \rho_{\mathbf{Q}_2} \rho_{-\mathbf{Q}_2}} \times [\cos(\Phi_1 - \Phi_2) + K_1 \cos \Phi_1 + K_2 \cos \Phi_2], \quad (\text{B1})$$

where

$$K_1 = \sqrt{\frac{\rho_{\mathbf{Q}_3} \rho_{-\mathbf{Q}_3}}{\rho_{\mathbf{Q}_2} \rho_{-\mathbf{Q}_2}}}, \quad K_2 = \sqrt{\frac{\rho_{\mathbf{Q}_3} \rho_{-\mathbf{Q}_3}}{\rho_{\mathbf{Q}_1} \rho_{-\mathbf{Q}_1}}}. \quad (\text{B2})$$

Differentiation of  $E_{\text{eff},5}$  with respect to  $\Phi_n$  ( $n = 1, 2$ ) leads to either

$$\cos \Phi_1 = \frac{K_2^2 - K_1^2 K_2^2 - K_1^2}{2K_1^2 K_2}, \quad \cos \Phi_2 = \frac{K_1^2 - K_1^2 K_2^2 - K_2^2}{2K_1 K_2^2}, \quad (\text{B3})$$

or

$$\sin \Phi_1 = \sin \Phi_2 = 0. \quad (\text{B4})$$

In the first case (B3),  $E_{\text{eff},5} = -\Gamma_5 \sum_n \rho_{\mathbf{Q}_n} \rho_{-\mathbf{Q}_n}$  follows, and a simple optimization of

$$\begin{aligned} E_{\text{eff}} &= -\mu \sum_n (\rho_{\mathbf{Q}_n} + \rho_{-\mathbf{Q}_n}) + \frac{\Gamma_1}{2} \sum_n (\rho_{\mathbf{Q}_n}^2 + \rho_{-\mathbf{Q}_n}^2) \\ &+ (\Gamma_2 - \Gamma_5) \sum_n \rho_{\mathbf{Q}_n} \rho_{-\mathbf{Q}_n} + \Gamma_3 \sum_{n < m} (\rho_{\mathbf{Q}_n} \rho_{\mathbf{Q}_m} + \rho_{-\mathbf{Q}_n} \rho_{-\mathbf{Q}_m}) \\ &+ \Gamma_4 \sum_{n < m} (\rho_{\mathbf{Q}_n} \rho_{-\mathbf{Q}_m} + \rho_{-\mathbf{Q}_n} \rho_{\mathbf{Q}_m}) \end{aligned} \quad (\text{B5})$$

leads to the vortex crystal solutions.

The other case (B4) corresponds to the state No. 10, where two of  $\Phi_n$  ( $1 \leq n \leq 3$ ) are equal and the third one differs from them by  $\pi$ . Numerical analysis of Eq. (4) suggests a certain symmetry among  $\rho_{\pm \mathbf{Q}_n}$  for this state:  $\rho_{\mathbf{Q}_1} = \rho_{-\mathbf{Q}_1} = p''\rho$ ,  $\rho_{\mathbf{Q}_2} = \rho_{-\mathbf{Q}_2} = q''\rho$ , and  $\rho_{\mathbf{Q}_3} = \rho_{-\mathbf{Q}_3} = r''\rho$  (or any equivalent distribution obtained by a symmetry operation) as is given in Table I. The effective energy density is

$$\begin{aligned} E_{\text{eff}} &= -2\mu(2x + z) + 4(\Gamma_1 + \Gamma_4)x^2 \\ &- 2(\Gamma_1 - \Gamma_2 - \Gamma_3 + \Gamma_4 - \Gamma_5)y^2 + (\Gamma_1 + \Gamma_2)z^2 \\ &- 4\Gamma_5 yz + 4(\Gamma_3 + \Gamma_4)zx, \end{aligned} \quad (\text{B6})$$

where  $x = (q'' + r'')\rho/2$ ,  $y = \sqrt{q''r''}\rho$ , and  $z = p''\rho$ . By differentiating this expression with respect to these variables we obtain

$$p'' = \frac{-\Gamma_1 + \Gamma_2 + \Gamma_3 - \Gamma_4 + \Gamma_5}{\Gamma_5} \sqrt{q''r''}, \quad (\text{B7})$$

TABLE I: Coefficients of the multi- $\mathbf{Q}$  states  $\langle \tau_i \rangle = \sum_n [c_n \exp(i\mathbf{Q}_n \cdot \mathbf{r}_i) + \bar{c}_n \exp(-i\mathbf{Q}_n \cdot \mathbf{r}_i)]$ . Equivalent states under symmetry are omitted. The indices of states are given in Fig. 3. For the state No. 5,  $p = (\Gamma_1 + \Gamma_3 - 2\Gamma_4)/(3\Gamma_1 + \Gamma_3 - 4\Gamma_4)$  and  $q = (1 - p)/2$  are required. For the state No. 9,  $p' = c(\Gamma_1 + \Gamma_2 - \Gamma_3 - \Gamma_4 - \Gamma_5)(\Gamma_1 - \Gamma_2 + \Gamma_3 - \Gamma_4 + \Gamma_5)$ ,  $q' = c[\Gamma_1^2 - (\Gamma_3 - \Gamma_4)^2 + \Gamma_2\Gamma_4 - \Gamma_1(\Gamma_2 + \Gamma_4 - \Gamma_5) - \Gamma_4\Gamma_5]$ , and  $r' = c(\Gamma_1 - \Gamma_3)(\Gamma_1 - \Gamma_2 + 2\Gamma_3 - 2\Gamma_4 + \Gamma_5)$  are required where  $c$  is determined by  $p' + 2q' + 2r' = 1$ . For the state No. 10, conditions for  $p''$ ,  $q''$ , and  $r''$  are obtained by solving Eqs. (B7) and (B8) along with  $p'' + q'' + r'' = 1/2$ . For the state No. 11,  $p''' = (\Gamma_1 + \Gamma_2 - \Gamma_3 - \Gamma_4)/(4\Gamma_1 + 2\Gamma_2 - 4\Gamma_3 - 2\Gamma_4)$  and  $q''' = 1/2 - p'''$  are required. The phase variables of states Nos. 7, 8, and 10 must satisfy  $\Theta = -3\Phi + 2\phi + 2\phi' = 0$  or  $\pi \pmod{2\pi}$ ; see Eq. (7) and the associated discussion. The phase variables are otherwise arbitrary.

State	$c_1$	$\bar{c}_1$	$c_2$	$\bar{c}_2$	$c_3$	$\bar{c}_3$
1	$\sqrt{\rho}$	0	0	0	0	0
2	$\sqrt{\rho/2}$	$\sqrt{\rho/2} e^{i\phi}$	0	0	0	0
3	$\sqrt{\rho/2}$	0	0	$\sqrt{\rho/2} e^{i\phi}$	0	0
4	$\sqrt{\rho/3}$	0	$\sqrt{\rho/3} e^{i\phi}$	0	$\sqrt{\rho/3} e^{i\phi'}$	0
5	$\sqrt{p\rho}$	0	0	$\sqrt{q\rho} e^{i\phi}$	0	$\sqrt{q\rho} e^{i\phi'}$
6	$\sqrt{\rho/4}$	$\sqrt{\rho/4} e^{i\Phi}$	$\sqrt{\rho/4} e^{i\phi}$	$\sqrt{\rho/4} e^{i(\Phi+\pi-\phi)}$	0	0
7	$\sqrt{\rho/6}$	$\sqrt{\rho/6} e^{i\Phi}$	$\sqrt{\rho/6} e^{i\phi}$	$\sqrt{\rho/6} e^{i(\Phi-\phi)}$	$\sqrt{\rho/6} e^{i\phi'}$	$\sqrt{\rho/6} e^{i(\Phi-\phi')}$
8	$\sqrt{\rho/6}$	$\sqrt{\rho/6} e^{i\Phi}$	$\sqrt{\rho/6} e^{i\phi}$	$\sqrt{\rho/6} e^{i(\Phi \pm 2\pi/3 - \phi)}$	$\sqrt{\rho/6} e^{i\phi'}$	$\sqrt{\rho/6} e^{i(\Phi \mp 2\pi/3 - \phi')}$
9	$\sqrt{p'\rho}$	0	$\sqrt{q'\rho} e^{i\phi}$	$\sqrt{r'\rho} e^{i(\Phi-\phi)}$	$\sqrt{q'\rho} e^{i\phi'}$	$\sqrt{r'\rho} e^{i(\Phi+\pi-\phi')}$
10	$\sqrt{p''\rho}$	$\sqrt{p''\rho} e^{i\Phi}$	$\sqrt{q''\rho} e^{i\phi'}$	$\sqrt{r''\rho} e^{i(\Phi+\pi-\phi')}$	$\sqrt{r''\rho} e^{i\phi''}$	$\sqrt{q''\rho} e^{i(\Phi+\pi-\phi'')}$
11	$\sqrt{p'''\rho}$	$\sqrt{p'''\rho} e^{i\phi}$	0	$\sqrt{q'''\rho} e^{i\phi''}$	$\sqrt{q'''\rho} e^{i\phi''}$	0

and

#### Acknowledgments

$$\begin{pmatrix} \Gamma_1 + \Gamma_4 & \frac{(\Gamma_3 + \Gamma_4)(-\Gamma_1 + \Gamma_2 + \Gamma_3 - \Gamma_4 + \Gamma_5)}{\Gamma_5} \\ \Gamma_3 + \Gamma_4 & \frac{(\Gamma_1 + \Gamma_2)(-\Gamma_1 + \Gamma_2 + \Gamma_3 - \Gamma_4 + \Gamma_5)}{\Gamma_5} - 2\Gamma_5 \end{pmatrix} \begin{pmatrix} q'' + r'' \\ \sqrt{q''r''} \end{pmatrix} = \begin{pmatrix} \mu \\ \mu \end{pmatrix}. \quad (\text{B8})$$

$p''$ ,  $q''$ , and  $r''$  can be obtained from Eqs. (B7) and (B8) along with the condition  $p'' + q'' + r'' = 1/2$ .

Work at LANL was performed under the auspices of the U.S. DOE Contract No. DE-AC52-06NA25396 through the LDRD program.

- <sup>1</sup> S. Mühlbauer, B. Binz, F. Jonietz, C. Pfleiderer, A. Rosch, A. Neubauer, R. Georgii, and P. Böni, *Science* **323**, 915 (2009).
- <sup>2</sup> W. Münzer, A. Neubauer, T. Adams, S. Mühlbauer, C. Franz, F. Jonietz, R. Georgii, P. Böni, B. Pedersen, M. Schmidt, et al., *Phys. Rev. B* **81**, 041203 (2010).
- <sup>3</sup> X. Yu, Y. Onose, N. Kanazawa, J. Park, J. Han, Y. Matsui, N. Nagaosa, and Y. Tokura, *Nature* **465**, 901 (2010).
- <sup>4</sup> S. Seki, X. Z. Yu, S. Ishiwata, and Y. Tokura, *Science* **336**, 198 (2012).
- <sup>5</sup> S. Seki, S. Ishiwata, and Y. Tokura, *Phys. Rev. B* **86**, 060403 (2012).
- <sup>6</sup> T. Giamarchi, C. Rüegg, and O. Tchernyshyov, *Nature Phys.* **4**, 198 (2008).
- <sup>7</sup> T. Nikuni, M. Oshikawa, A. Oosawa, and H. Tanaka, *Phys. Rev. Lett.* **84**, 5868 (2000).
- <sup>8</sup> M. Matsumoto, B. Normand, T. M. Rice, and M. Sigrist, *Phys. Rev. Lett.* **89**, 077203 (2002).
- <sup>9</sup> C. Rüegg, N. Cavadini, A. Furrer, H. Güdel, K. Krämer, H. Mutka, A. Wildes, K. Habicht, and P. Vorderwisch, *Nature* **423**, 62 (2003).
- <sup>10</sup> H. Kageyama, K. Yoshimura, R. Stern, N. V. Mushnikov, K. Onizuka, M. Kato, K. Kosuge, C. P. Slichter, T. Goto, and Y. Ueda, *Phys. Rev. Lett.* **82**, 3168 (1999).
- <sup>11</sup> K. Kodama, M. Takigawa, M. Horvatic, C. Berthier, H. Kageyama, Y. Ueda, S. Miyahara, F. Becca, and F. Mila, *Science* **298**, 395 (2002).
- <sup>12</sup> S. E. Sebastian, N. Harrison, P. Sengupta, C. D. Batista, S. Francoual, E. Palm, T. Murphy, N. Marcano, H. A. Dabkowska, and B. D. Gaulin, *Proc. Natl. Acad. Sci. USA* **105**, 20157 (2008).
- <sup>13</sup> S. E. Sebastian, N. Harrison, C. D. Batista, L. Balicas, M. Jaime, P. A. Sharma, N. Kawashima, and I. R. Fisher, *Nature (London)* **441**, 617 (2006).
- <sup>14</sup> C. D. Batista, J. Schmalian, N. Kawashima, P. Sengupta, S. E. Sebastian, N. Harrison, M. Jaime, and I. R. Fisher, *Phys. Rev. Lett.* **98**, 257201 (2007).
- <sup>15</sup> Y. Kamiya, N. Kawashima, and C. D. Batista, *J. Phys. Soc. Jpn.* **78**, 094008 (2009).

- <sup>16</sup> Y. Kamiya, N. Kawashima, and C. D. Batista, Phys. Rev. B **82**, 054426 (2010).
- <sup>17</sup> M. Uchida, H. Tanaka, H. Mitamura, F. Ishikawa, and T. Goto, Phys. Rev. B **66**, 054429 (2002).
- <sup>18</sup> M. B. Stone, M. D. Lumsden, S. Chang, E. C. Samulon, C. D. Batista, and I. R. Fisher, Phys. Rev. Lett. **100**, 237201 (2008).
- <sup>19</sup> E. C. Samulon, Y.-J. Jo, P. Sengupta, C. D. Batista, M. Jaime, L. Balicas, and I. R. Fisher, Phys. Rev. B **77**, 214441 (2008).
- <sup>20</sup> E. C. Samulon, Y. Kohama, R. D. McDonald, M. C. Shapiro, K. A. Al-Hassanieh, C. D. Batista, M. Jaime, and I. R. Fisher, Phys. Rev. Lett. **103**, 047202 (2009).
- <sup>21</sup> E. C. Samulon, K. A. Al-Hassanieh, Y.-J. Jo, M. C. Shapiro, L. Balicas, C. D. Batista, and I. R. Fisher, Phys. Rev. B **81**, 104421 (2010).
- <sup>22</sup> S. Suh, K. A. Al-Hassanieh, E. C. Samulon, I. R. Fisher, S. E. Brown, and C. D. Batista, Phys. Rev. B **84**, 054413 (2011).
- <sup>23</sup> A. V. Chubukov and D. I. Golosov, J. Phys. Condens. Matter **3**, 69 (1991).
- <sup>24</sup> S. Sachdev and R. N. Bhatt, Phys. Rev. B **41**, 9323 (1990).
- <sup>25</sup> V. N. Kotov, O. Sushkov, Z. Weihong, and J. Oitmaa, Phys. Rev. Lett. **80**, 5790 (1998).
- <sup>26</sup> O. Rösch and M. Vojta, Phys. Rev. B **76**, 224408 (2007).
- <sup>27</sup> S. T. Beliaev, Sov. Phys. JETP **7**, 299 (1958).
- <sup>28</sup> T. Nikuni and H. Shiba, J. Phys. Soc. Jpn. **64**, 3471 (1995).
- <sup>29</sup> G. Jackeli and M. E. Zhitomirsky, Phys. Rev. Lett. **93**, 017201 (2004).
- <sup>30</sup> H. T. Ueda and K. Totsuka, Phys. Rev. B **80**, 014417 (2009).
- <sup>31</sup> T. Matsubara and H. Matsuda, Prog. Theor. Phys. **16**, 569 (1956).
- <sup>32</sup> T. Okubo, S. Chung, and H. Kawamura, Phys. Rev. Lett. **108**, 017206 (2012).
- <sup>33</sup> I. Rousochatzakis, U. K. Rössler, J. van den Brink, and M. Daghofer, arXiv:1209.5895 (unpublished).
- <sup>34</sup> Y. Kamiya and C. D. Batista, Phys. Rev. Lett. **109**, 067204 (2012).
- <sup>35</sup> W. Selke, Phys. Rep. **170**, 213 (1988).
- <sup>36</sup> P. Bak, Rep. Prog. Phys. **45**, 587 (1982).
- <sup>37</sup> A. Abrikosov, Sov. Phys. JETP **5**, 1174 (1957).
- <sup>38</sup> M. H. Whitmore, H. R. Verdún, and D. J. Singel, Phys. Rev. B **47**, 11479 (1993).